



# Redox potentials of pollutants determining the dominate oxidation pathways in manganese single-atom catalyst (Mn-SAC)/peroxymonosulfate system: Selective catalytic mechanisms for versatile pollutants

Kexin Yin<sup>a</sup>, Yanan Shang<sup>a,b,\*</sup>, Dongdong Chen<sup>a</sup>, Baoyu Gao<sup>a</sup>, Qinyan Yue<sup>a</sup>, Xing Xu<sup>a,c,\*\*</sup>

<sup>a</sup> Shandong Key Laboratory of Water Pollution Control and Resource Reuse, School of Environmental Science and Engineering, Shandong University, Qingdao 266237, PR China

<sup>b</sup> College of Safety and Environmental Engineering, Shandong University of Science and Technology, Qingdao 266590, PR China

<sup>c</sup> Civil Engineering, College of Science and Engineering, National University of Ireland, Galway H91 TK33, Ireland

## ARTICLE INFO

### Keywords:

Redox potentials  
Fenton-like system  
Single-atom  
Manganese  
Selective catalysis

## ABSTRACT

Versatile persulfate-based catalytic mechanisms induced by highly-effective single atom catalysts (SACs) have been intensively reported, which was mainly ascribed to the versatile coordinated-structures of SACs. However, the origin of these different mechanisms from the specific properties of pollutants has been ignored. In this work, eight kinds of pollutants were selected and the half-wave potential ( $\phi_{1/2}$ ) values representing their redox potentials were determined. A good correlation between the redox potential characteristics of pollutants and their oxidation performances/pathways in manganese single-atom catalyst (Mn-SAC)/PMS system can be confirmed. The  $\phi_{1/2}$  values of different pollutants showed a good correlation with the energy gaps between the pollutants and Mn-SAC/PMS complexes as well as their electrophilicity indexes, which confirmed the redox potential of pollutants was essential to the electron-transfer oxidation in Mn-SAC/PMS system. Based on the new insights in this work, we will be able to unveil the sources of Fenton-like systems with tunable oxidation processes.

## 1. Introduction

Advanced oxidation processes (AOPs), which can produce a large mass of reactive oxidative species with high oxidation activity for decomposing the organic pollutants, have become an irreplaceable technique in wastewater treatment [1–5]. Recently, activation of persulfate (peroxymonosulfate (PMS), and peroxodisulfate (PDS)) by transition metal species has attracted promising attention due to their higher efficiency with lower energy requirement [6–9]. Most of homogeneous transition-metal catalysts showed high activity and high selectivity to organics, but are impeded by difficulties in separation from the catalytic systems and sludge generation/agglomerations for disposal [10–12]. Heterogeneous transition-metal catalysts attracted increasing interest for their high stability, facile separation and recycling, but the utilization of metal atoms is low because most of the atoms are buried in the bulks [13, 14].

Single-atom catalysts (SACs) show the merits of both heterogeneous

and homogeneous transition-metal catalysts, which maximize atomic utilization by immobilizing single metal atoms on the substrate to fully expose the catalytic sites [7,15,16]. As compared with the radical-dominated catalytic mechanisms in heterogeneous SACs/H<sub>2</sub>O<sub>2</sub> systems [17–19], the mechanisms in heterogeneous SACs/persulfate systems are always diverse because of the versatile persulfate activation pathways triggered by a variety of metal centers with different coordination configurations [20–22]. SACs normally activate PMS or PDS, inducing radicals, nonradical pathways, or a combined radical/nonradical pathways [23–25]. However, some contradictory catalytic mechanisms via PMS activation by the same coordination structure of SACs have been always reported, which is somewhat confusing [26–30]. For example, the degradation of sulfamethoxazole was mainly contributed by free radicals [26], while Fe(V) species were reported as the dominated active oxidant for bisphenol A degradation during the activation of PMS by the Fe-N<sub>4</sub>-C catalyst [27]. Other Fe-N<sub>4</sub>-C catalysts also exhibited the electron-transfer or <sup>1</sup>O<sub>2</sub> dominated pathways for targeted

\* Corresponding author at: College of Safety and Environmental Engineering, Shandong University of Science and Technology, Qingdao 266590, PR China.

\*\* Corresponding author at: Shandong Key Laboratory of Water Pollution Control and Resource Reuse, School of Environmental Science and Engineering, Shandong University, Qingdao 266237, PR China.

E-mail addresses: [shangyanan@sdu.edu.cn](mailto:shangyanan@sdu.edu.cn) (Y. Shang), [xuxing@sdu.edu.cn](mailto:xuxing@sdu.edu.cn) (X. Xu).

<https://doi.org/10.1016/j.apcatb.2023.123029>

Received 15 September 2022; Received in revised form 24 April 2023; Accepted 22 June 2023

Available online 24 June 2023

0926-3373/© 2023 Elsevier B.V. All rights reserved.

pollutants degradation via PMS activation [28–30]. In fact, not only the Fe-SACs, the Co-SACs and Mn-SACs with same coordination structures could also show different catalytic mechanisms for oxidating different targeted pollutants [19,31,32]. Therefore, the oxidation performance and mechanisms in different SACs/PMS systems should be considered not only from the versatile coordinated-structures (e.g., coordination numbers, metal centers, and metal-supports interactions) of SACs, but also from the specific characteristics of targeted pollutants [33]. However, recent studies mainly focused on the coordinated-structures of SACs to explain the different catalytic mechanisms [27–33], but the origin of these different mechanisms from the specific properties of pollutants has been ignored, let alone establish the relationship between the specific properties of pollutants and oxidation performance/pathways in SACs/PMS systems. Our previous work first reported that the metronidazole (MNZ) with a high redox potential could be primarily oxidized by free radicals in Co-N<sub>4</sub>-C/PMS system, while the oxidation of bisphenol A (BPA) with low-redox was dominated by electron transfer process (ETP) [10]. However, whether the redox potential values of different pollutants can exhibit a certain correlation with the properties of SACs/PMS complexes that well reflected the oxidation pathways for different pollutants was still unclear. Therefore, it was necessary to study the correlation between the redox potential values of pollutants and the properties of SACs/PMS complexes in the SACs/PMS systems, so as to establish SACs/PMS systems with variable selectivity and tunable oxidation capacity for the decontamination of pollutants.

As a result, the aim of this study was to illustrate the origin of selective degradation of targeted pollutants in the SACs/PMS systems from the prospective of specific properties of pollutants. A manganese single-atom catalyst (Mn-SAC) with high Mn loading was fabricated via a pyrolysis process using the lignin as the parent material and characterized by various techniques. First, the mechanisms of different pollutants were investigated in the Mn-SAC/PMS systems. Second, the half-wave potential ( $\varphi_{1/2}$ ) of different pollutants was evaluated and the relationship between  $\varphi_{1/2}$  and the dominate oxidation pathways of pollutants was evaluated. Third, DFT calculation were employed to further investigate the origin of different mechanisms from the specific properties of pollutants in the Mn-SAC/PMS systems. Moreover, the transformation products of pollutants in the Mn-SAC/PMS systems and the degradation of contaminants in catalytic filter systems were also assessed.

## 2. Materials and methods

### 2.1. Chemicals

The lignin was extracted from the reed in the wetland of Nansi Lake in Shandong Province (Detailed extraction method in Appendix S1 and Fig. S1). The chemical materials, including KHSO<sub>5</sub>·0.5KHSO<sub>4</sub>·0.5 K<sub>2</sub>SO<sub>4</sub> (PMS), MnCl<sub>2</sub>·4 H<sub>2</sub>O, Zn(NO<sub>3</sub>)<sub>2</sub>·6 H<sub>2</sub>O, ethylene diamine tetraacetic acid (EDTA), dicyandiamide, MnO, Mn<sub>2</sub>O<sub>3</sub>, FeSO<sub>4</sub>·7 H<sub>2</sub>O, N,N-Diethyl-p-phenylenediamine sulfate salt, Na<sub>2</sub>SO<sub>4</sub>, N,N-dimethylformamide, ethanol (EtOH), tert-butyl alcohol (TBA), 5,5-dimethylpyrroline-oxide (DMPO), carbon felt, Nafion perfluorinated resin were obtained from Sinopharm Chemical Reagent Co. Ltd. All pollutants used in this work, e.g., bisphenol A (BPA), p-chlorophenol (CP), metronidazole (MNZ), carbamazepine (CBZ), sulfamethoxazole (SMX), p-nitrophenol (PNP), chloramphenicol (CPL), sulfanilamide (SA), were purchased from Aladdin Co. Ltd., China.

### 2.2. Preparation of lignin-based Mn-SAC catalyst

The lignin-based Mn-SAC catalyst was prepared by four steps as follows. (i) The reed-derived lignin (4.0 g) and EDTA (2.0 g) were first mixed with 500 ml of deionized water, and then MnCl<sub>2</sub>·4 H<sub>2</sub>O (28 mmol) and Zn(NO<sub>3</sub>)<sub>2</sub>·6 H<sub>2</sub>O (28 mmol) were added into the lignin solution, stirring for 60 min and standing for overnight. (ii) The Mn/Zn-lignin complex was separated via filtration, and dried for 12 h at 80 °C. It

was then fully grinded to ground and mixed with 10 times weight of dicyandiamide. (iii) The mixture was put into a quartz boat and pyrolyzed in a tubular furnace at 550 °C for 1 h and 1000 °C for another 1 h under N<sub>2</sub> atmosphere. Zn atoms help disperse the Mn atoms in the carbon framework and they are evaporated with temperature higher than 900 °C. The properties (e.g., coordination structures, microstructures, metal content) of the Mn-SAC catalyst were determined by various measurements, which were given in Appendix S2.

### 2.3. Experimental procedure

The degradation of eight pollutants, including BPA, CP, MNZ, CBZ, SMX, PNP, CPL, and SA, was first conducted by adding 5 mg of Mn-SAC with PMS (4.0 mM) into 50 ml of pollutant solutions. Conventional homogeneous and heterogeneous tests using Mn<sup>2+</sup> (with amount equal to the Mn amount of Mn-SAC added in the system), and MnO were carried out. The solution (1 ml) was withdrawn at required time interval and filtered via a 0.22 μm film. The filtrate was mixed with 0.5 ml methanol to quench the radicals, and then the residual concentrations of pollutants were determined by a high-performance liquid chromatograph (HPLC, UltiMate 3000) with a C-18 column (Table S1). Degradation of the above pollutants with 0, 0.5, 2.0 and 4.0 mM of PMS by the addition of 5 mg of Mn-SAC were also conducted. All degradation tests were conducted at natural pH (specific pH is shown in Table S2). In addition, the reactive oxygen species (ROS) in the Mn-SAC/PMS system were determined by adding the scavengers (e.g., TBA (200 mM), and EtOH (200 mM)) into the catalytic systems. D<sub>2</sub>O as solution was employed to replace the H<sub>2</sub>O for determining the role of singlet oxygen (<sup>1</sup>O<sub>2</sub>).

Other experimental procedures, including electrochemical measurements (cyclic voltammetry, and open circuit potential), galvanic oxidation system, electron paramagnetic resonance (EPR), residual PMS detection, extraction tests were given in Appendix S3–S7.

### 2.4. DFT calculation

Molclus 1.9.9.9 was employed for conformational searching [34], and then the resulted lowest energy conformers were optimized using DFT at dispersion correction B3LYP-D3(BJ) and basis set B3LYP-D3/6-31 + G(d) with Gaussian 09 program [35,36]. Frequency calculations was conducted at the same level to make sure no imaginary frequency existing so that the conformers were converged to a local minimum. For single-point energy calculations, natural population analysis (NPA) charges, highest occupied molecular orbitals (HOMO)/lowest unoccupied molecular orbital (LUMO), softness, hardness, and electrophilicity index, B3LYP-D3(BJ) and better basis set 6-311 + +G(d,p) were used [35]. Multiwfn 3.8, a wavefunction analysis program, was used for further analysis [37]. Meanwhile, SMD solvation model was applied to take solvent effect (in water) into account [38].

## 3. Results and discussions

### 3.1. Characteristics of lignin-based Mn-SAC catalyst

The surface and coordination properties of lignin-based Mn-SAC catalyst was characterized by various techniques [39,40]. Transmission electron microscopy (TEM) image of the Mn-SAC catalyst showed that there were no nanoparticles embedded in the carbon matrixes (Fig. 1a and Fig. S2), indicating that no Mn species were aggregated; this was also consistent with the XRD pattern of the Mn-SAC catalyst (Fig. S3). The high-angle annular dark-field scanning transmission electron microscopy (HAADF-STEM) image visualized the uniform light spots in the carbon carriers (Fig. 1b and c), and its EDS mappings indicated the well distributed Mn species with Mn content of 4.07 wt% (Fig. S4).

X-ray absorption spectroscopy (XAS) could give various detailed coordination information of the as-prepared SACs, e.g., coordination

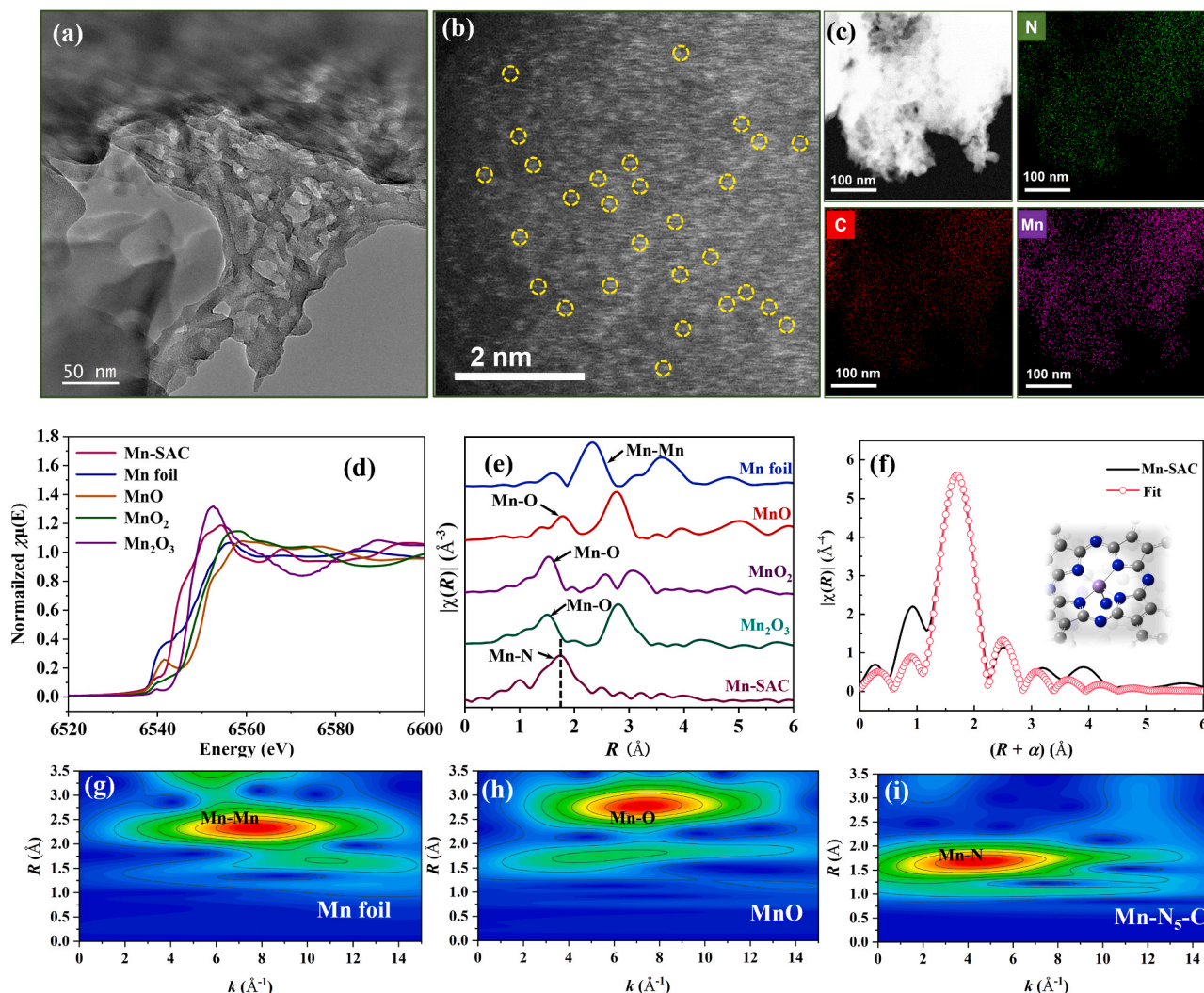


**Fig. 1.** (a) TEM image of the Mn-SAC catalyst; (b) HAADF-STEM image of the Mn-SAC catalyst and (c) its EDS mappings; (d) XANES of Mn-SAC catalyst; (e) FT-EXAFS of Mn-SAC catalyst; (f) EXAFS fitting of Mn-SAC catalyst; WT-EXAFS spectra of (g) Mn foil; (h) MnO; (i) Mn-SAC.

structure, chemical/bonding states [41,42]. The X-ray absorption near-edge structure (XANES) of Mn-SAC showcased that the absorption edge of Mn single-atom was located between the MnO and MnO<sub>2</sub> (Fig. 1d), showing the valence state of Mn single-atom between Mn(II) and Mn(III). The Fourier transform extended X-ray absorption fine structure (FT-EXAFS) unveiled that the prominent peak of Mn-SAC was located at 1.67 Å (Fig. 1e), which was quite different from the specific peaks of Mn-Mn and Mn-O. This indicated that the single-atom Mn was exclusively coordinated with the N atoms in the Mn-SAC. The Mn-N coordination number was calculated to be 4.97 according to the EXAFS fitting (Fig. 1f and Table S3), which indicated that the Mn-N<sub>5</sub> configuration was the dominated coordination structure in Mn-SAC. Natural population analysis (NPA) showed that Mn atom in the center of Mn-N<sub>5</sub> was positively charged (Fig. S7). The wavelet transform (WT) of EXAFS (WT-EXAFS) allowed the resolution of backscattered atoms with the information of elemental nature and radius distance at both R- and k-spaces, respectively. The WT-EXAFS spectra showed the maximum intensity at 4.4 Å<sup>-1</sup>, which was associated to the Mn-N bond as comparing with the Mn foil, and MnO (Fig. 1g-i). As a result, an integrated FT and WT EXAFS analysis confirmed the atomically-dispersed Mn site in the as-prepared Mn-SAC and further provided its precise coordination environment.

### 3.2. Oxidation of different pollutants in Mn-SAC/PMS system

Oxidation of different pollutants (e.g., BPA, CP, CBZ, PNP, BA, SMX, MNZ and CPL) by PMS alone (4.0 mM), Mn<sup>2+</sup>/PMS, MnO/PMS, and Mn-SAC/PMS systems were shown in Fig. 2. The PMS alone system achieved different oxidation selectivity towards pollutants. For example, approximately 50% of BPA, 40% of SMX, and 15–20% of CP and CBZ could be oxidized by the PMS alone, while the degradation of MNZ and PNP could not be detected (Fig. 2a). In addition, adding the Mn<sup>2+</sup> (the same Mn amount in the Mn-SAC), and MnO only provided a very small contribution to the oxidation of pollutants (Fig. 2b and c). In contrast, the degradation of all pollutants could be greatly improved by the addition of Mn-SAC catalyst (Fig. 2d), with the *k*<sub>obs</sub> values two or three orders of magnitude higher than those of PMS alone, Mn<sup>2+</sup>/PMS, MnO/PMS and other catalytic systems (Fig. 2e and Table S4). These results indicated that the Mn-SAC catalyst with high content of Mn atomic sites could guarantee the maximum catalytic capacity for the oxidation of different organics. However, the degradation of these pollutants showed three *k*<sub>obs</sub> regions (pollutants of BPA and CP with high *k*<sub>obs</sub>, pollutants of SA, SMX, CBZ and PNP with moderate *k*<sub>obs</sub>, and pollutants of MNZ and CPL with low *k*<sub>obs</sub>) in Mn-SAC/PMS system (Fig. 2e), which need to be further clarified.

Degradation of different pollutants by the Mn-SAC with various PMS dosages (0, 0.5, 2.0, and 4.0 mM) was shown in Fig. 3. The Mn-SAC



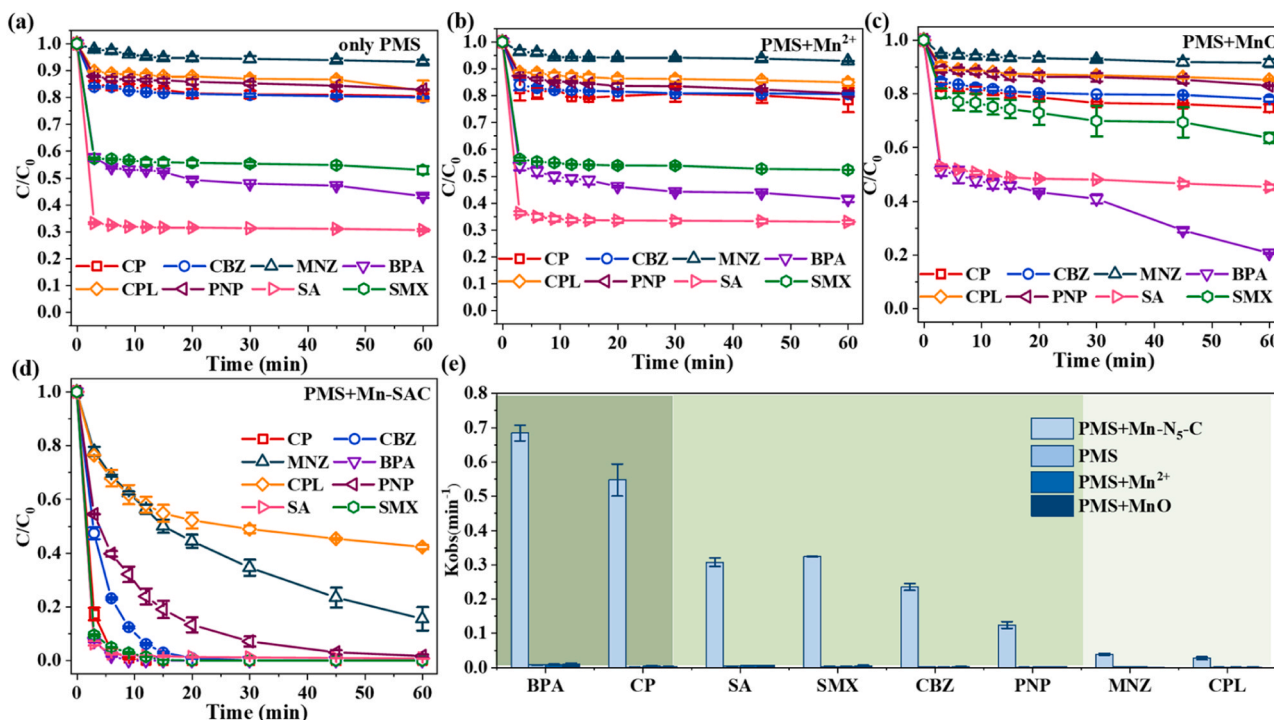


Fig. 2. Oxidation of different pollutants in (a) PMS alone (4.0 mM), (b)  $\text{Mn}^{2+}$ /PMS, (c)  $\text{MnO}$ /PMS, and (d)  $\text{Mn-SAC}$ /PMS systems; (e) The  $k_{\text{obs}}$  values in PMS alone,  $\text{Mn}^{2+}$ /PMS,  $\text{MnO}$ /PMS, and  $\text{Mn-SAC}$ /PMS systems. (Catalyst dosage: 0.1 g/L; PMS dosage: 4 mM; pollutants concentration: 10 mg/L).

catalyst could adsorb 75% of BPA, and approximately 10–30% of other pollutants.  $\text{Mn-SAC}$  exhibited a large surface area and pore structure (Fig. S8 and Table S5), which may provide more opportunities for the adsorption of PMS and pollutants. The residual pollutants (e.g., BPA, and CP) attached on the  $\text{Mn-SAC}$  after PMS activation was extracted, and only approximately 1–2% of BPA and CP can be extracted from the spent  $\text{Mn-SAC}$  at different time intervals; this result indicated that the residual pollutants can be further oxidized after the surface enrichment (Fig. S9). This would also affect the catalytic stability since the intermediates would be adsorbed onto the surface of  $\text{Mn-SAC}$  catalyst to saturate the reactive sites. As a result, the degradation rate of NPX was gradually decreased although 100% of NPX oxidation still can be achieved by the  $\text{Mn-SAC}$  after several cycles (Fig. S10a and S10b). While there was a significant increase in its oxidation capacity when we pyrolyzed the used  $\text{Mn-SAC}$  at a lower pyrolysis temperature (350 °C) due to the decomposition of these intermediates.

In the  $\text{Mn-SAC}$ /PMS system, it was obvious that different pollutants showcased different degradation rates and their  $k_{\text{obs}}$  values were also quite close to the PMS dosages. For example, BPA and CP could be completely oxidized within 10 min at PMS dosage of 0.5 mM, and the further increase of PMS only showed a small increase in  $k_{\text{obs}}$ . In contrast, CBZ, PNP, BA and SMX showed a relatively lower oxidation rate at PMS dosage of 0.5 mM, while the 100% of degradation can be achieved at PMS dosage of 4.0 mM with  $k_{\text{obs}}$  increasing 2–4 times. What's more, the  $\text{Mn-SAC}$  catalyst exhibited neglectable oxidation activity ( $<0.001 \text{ min}^{-1}$ ) for the refractory MNZ and CPL at low PMS dosage, and the degradation rate could increase to  $0.02 \text{ min}^{-1}$  with the increasing PMS dosage to 4.0 mM. Such results exhibited the oxidation selectivity of the pollutants in the  $\text{Mn-SAC}$ /PMS system, and the oxidation of refractory organics could be improved by increasing PMS dosage. Increasing  $\text{Mn-SAC}$  dosage could also promote the catalytic performance for different pollutants in  $\text{Mn-SAC}$ /PMS system, but showed less effect as compared with the PMS dosage, especially for the refractory MNZ and CPL (Fig. S11).

Basically, three kinds of oxidation trends for different pollutants can be identified as: organics with high oxidation rate at low PMS dosage

(CP as example), organics with high oxidation rate at high PMS dosage (CBZ as example), and refractory organics with enhanced oxidation rate at high PMS dosage (MNZ as example). The versatile degradation trends might be due to the different oxidation origins towards targeted pollutants.

### 3.3. Electrochemical property of different pollutants

The cyclic voltammetry (CV) can be used to identify the redox potentials of pollutants [43]. The half-wave potential ( $\phi_{1/2}$ ) of different pollutants can be evaluated from the peak 1a in the CV spectra (Fig. S12) of pollutants, which could represent the redox potential of the pollutants [43,44]. The BPA exhibited a lowest  $\phi_{1/2}$  value (0.495 V) among all selected pollutants, and it was followed by  $\text{CP} < \text{SA} < \text{SMX} < \text{CBZ} < \text{PNP} < \text{MNZ} < \text{CPL}$  (Fig. 4a). Relationship between the  $\phi_{1/2}$  values of different pollutants and their  $k_{\text{obs}}$  values obtained at different PMS dosages in  $\text{Mn-SAC}$ /PMS system were shown in Fig. 4b–d. It was obvious that the  $\phi_{1/2}$  values (lower than 1.2 V) of six pollutants (BPA, CP, SA, SMX, CBZ, and PNP) showed significant correlations with their  $\ln k_{\text{obs}}$ . In contrast, MNZ and CPL showed very low  $\ln k_{\text{obs}}$  values, which were deviated from the correlated lines. These results indicated that the oxidation of pollutants was closely related to their redox potentials. In addition, the  $\phi_{1/2}$  values of all eight pollutants can be classified into three intervals (low  $\phi_{1/2}$  values, moderate  $\phi_{1/2}$  values, and high  $\phi_{1/2}$  values as shown in Fig. 4b–d), with the intervals also corresponding well to the degradation rates of the classified pollutants as shown in Fig. 3e.

### 3.4. Versatile oxidation pathways for different pollutants in $\text{Mn-SAC}$ /PMS system

Three kinds (CP, CBZ, and MNZ) of typical pollutants were selected to represent the classified pollutants in low  $\phi_{1/2}$  interval, moderate  $\phi_{1/2}$  interval, and high  $\phi_{1/2}$  interval. Both adsorption and degradation of these pollutants at different pH conditions showed a small variation (Fig. S13 and S14), which indicated that the speciation of pollutants show little effect on the degradation. To identify the degradation



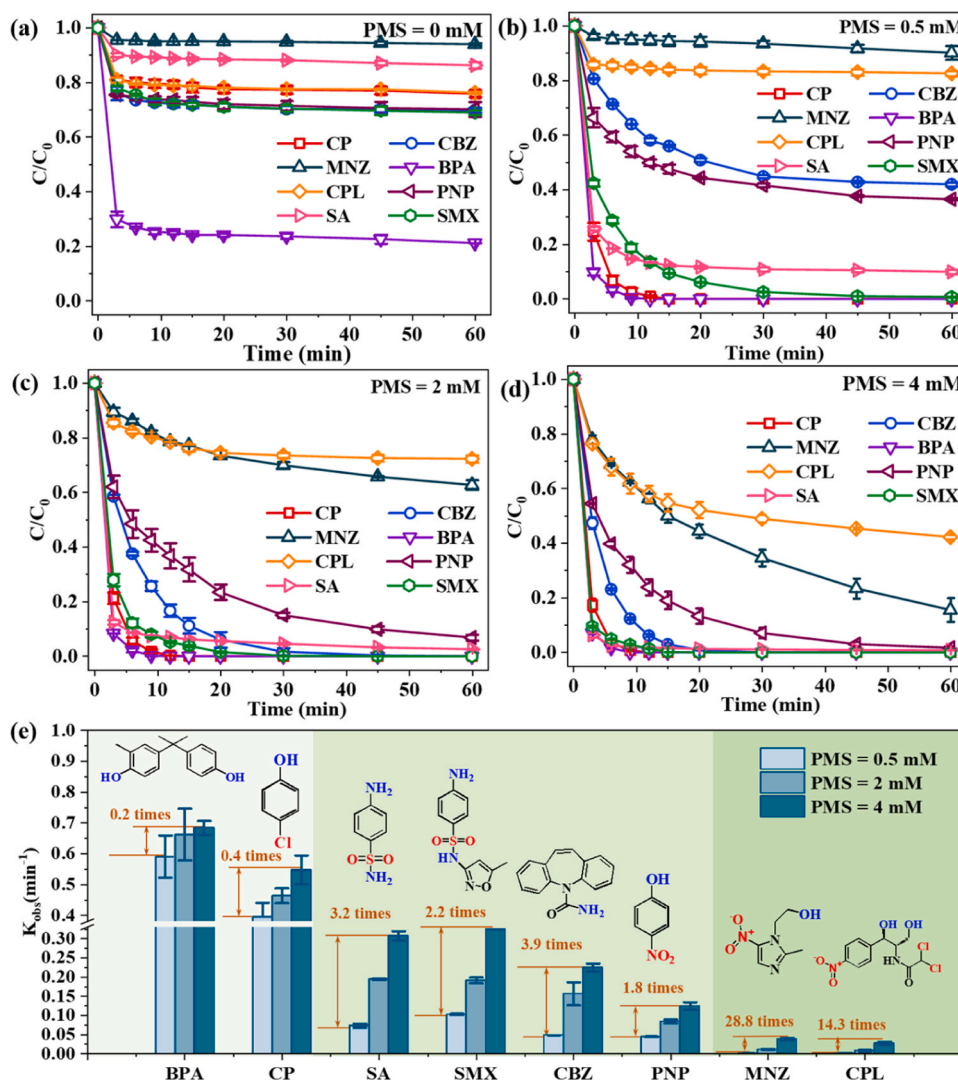


**Fig. 3.** (a) Adsorption of different pollutants by Mn-SAC; Oxidation of different pollutants in Mn-SAC/PMS system (b) at PMS dosage of 0.5 mM, (c) at PMS dosage of 2.0 mM, (d) at PMS dosage of 4.0 mM; (e) The  $k_{obs}$  values for different pollutants at different PMS dosages. (Catalyst dosage: 0.1 g/L; PMS dosage: 0.5–4.0 mM; pollutant concentrations: 10 mg/L).

pathways for the classified pollutants in Mn-SAC/PMS system, the contributions of ROS for the oxidation of CP, CBZ, and MNZ were accessed by the radical scavengers [45–48]. The addition of ethanol (EtOH) and tert-butyl alcohol (TBA) showed little influence on the oxidation of CP and CBZ (Fig. 5a and 5b, and Fig. S16). In contrast, MNZ oxidation was greatly restricted by the EtOH and TBA scavengers (Fig. 5c). These results indicated that free radicals were the dominating species for MNZ degradation in Mn-SAC/PMS system but their roles on the oxidation of CP and CBZ were relatively small. Similar quenching results for other contaminants (BPA, SA, SMX, PNP, and CPL) were also observed (Fig. S17). Both 2,2,6,6-tetramethyl-4-piperidinol (TEMP) and furfuryl alcohol (FFA) were used as the  $^1O_2$  scavengers for measuring the role of  $^1O_2$  in the oxidation of different pollutants [47–49]. The TEMP and FFA exhibited a very small effect on the CP degradation, while CBZ and MNZ degradation showed the converse results by the addition of FFA (Fig. 5a–d). Considering that both TEMP and FFA would consume the PMS which might mislead the quenching results, the residual PMS amounts in the catalytic systems with the addition of different quenching agents were determined (Fig. S18). It was obvious that the TEMP and FFA could consume more than 20% and 80% of PMS (original PMS concentration: 4.0 mM) within 10 min. Oxidation of CP could achieve high  $k_{obs}$  even at PMS dosage of 0.5 mM. In contrast, the  $k_{obs}$  of

CBZ and MNZ would be greatly reduced at lower PMS dosage. As a result, the quenching results using the  $^1O_2$  scavengers could not reflect the role of  $^1O_2$  in the oxidation of different pollutants.

The EPR technique using spin-trapping reagent of DMPO showed the typical DMPOX signals with the similar intensities in the Mn-SAC/PMS system regardless of the presence/absence of different pollutants (e.g., CP, CBZ, and MNZ), as shown in Fig. 5e and f. This indicated that the radicals have been produced in all catalytic systems that oxidized the DMPO into DMPOX [48,50]. However, this seemed to be in contradiction to the weak contribution of radicals in the oxidation of CP and CBZ. This might be due to the fact that the radicals did participate to the oxidation of CP and CBZ, but their roles in the oxidation of CP and CBZ were most likely covered up by other dominating pathways in the Mn-SAC/PMS system. In addition, increasing PMS dosage could promote the radical signals in the Mn-SAC/PMS system, confirming that the  $k_{obs}$  of MNZ could be effectively improved at higher PMS dosage (Fig. 5e). EPR spectra detected in the TEMP spin-trapping conditions suggested that  $^1O_2$  could be generated in the Mn-SAC/PMS system with/without the addition of targeted pollutants (Fig. 5g). It was known that the lifetime of  $^1O_2$  can be prolonged in D<sub>2</sub>O solution [43,51], but the degradation of CP, CBZ, and MNZ in the Mn-SAC/PMS system was not accelerated by replacement of H<sub>2</sub>O with D<sub>2</sub>O (Fig. 5h). This was

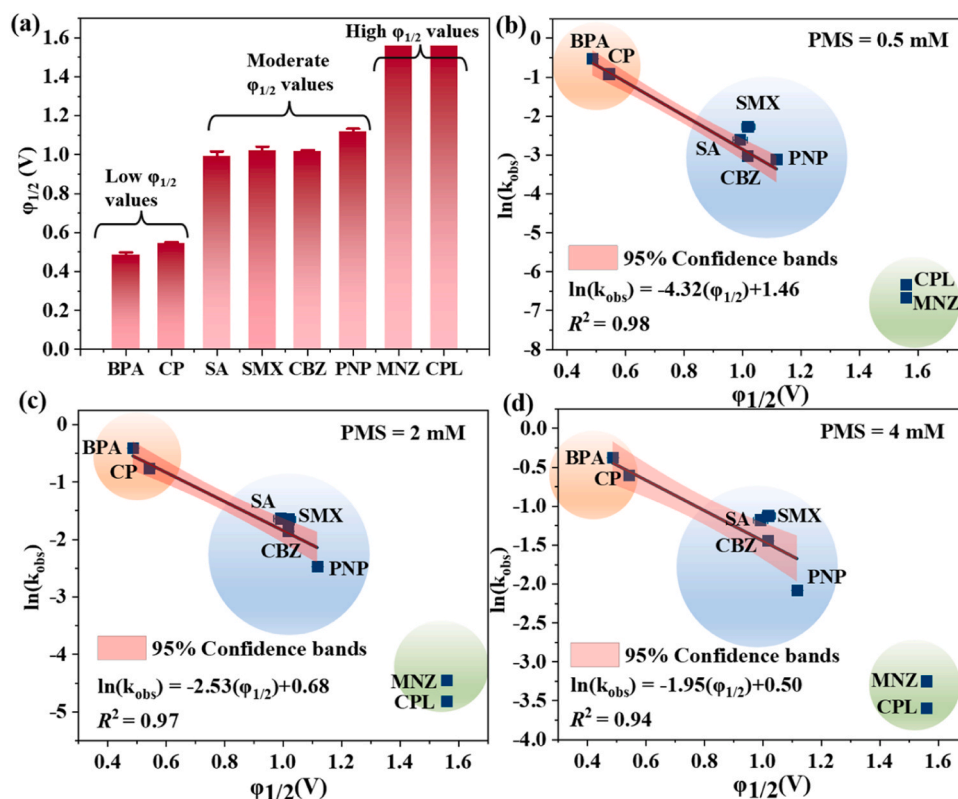


Fig. 4. (a) Calculated  $\phi_{1/2}$  values of eight contaminants; Relationship between  $\phi_{1/2}$  values of eight contaminants and their  $k_{obs}$  at PMS dosage of (b) 0.5 mM, (c) 2.0 mM, (d) 4.0 mM.

consistent with previous reports that  $^1\text{O}_2$  could be easily generated in the PMS-based reactions but always contributed a negligible role to the oxidation of organics [20,43,52]. Based on the combinations of electrochemical, quenching, and EPR analysis, it can be concluded that radicals were the dominating species for the oxidation of pollutants with high  $\phi_{1/2}$  values (e.g., MNZ). In contrast, although radicals were involved in the degradation of the pollutants with  $\phi_{1/2}$  values lower than 1.2 V (e.g., CP, and CBZ), their contributions were almost overlapped by other dominating nonradical pathways. As a result, the versatile catalytic pathways in the Mn-SAC/PMS system can be induced from the redox potential characteristics of pollutants, which were crucial to the degradation performances of pollutants.

The contributions of radicals and nonradical pathways for oxidating different pollutants in the Mn-SAC/PMS system were further evaluated by a premixing test via a premixture of Mn-SAC and PMS at designed time intervals before adding different pollutants, e.g., CP, CBZ, and MNZ [53,54]. If the degradation pathway was dominated by the electron-transfer via electron flowing between the catalyst and pollutants, the premixing of catalyst and PMS would show a small effect on the oxidation of pollutants [53,54]. Premixing the Mn-SAC and PMS for 3 and 6 min showed almost negligible inhibitive effect on the CP degradation (Fig. 6a), which indicated that the electron-transfer overwhelmed the effect of radicals in oxidating the CP. In contrast, the degradation of CBZ showed a noticeable decay effect with the  $k_{obs}$  of CBZ decreasing from  $0.232 \text{ min}^{-1}$  to  $0.155 \text{ min}^{-1}$  at the premixing time of 6 min (Fig. 6a and b). This result indicated that CBZ oxidation was mainly controlled by the electron-transfer in the Mn-SAC/PMS system but the contribution of radical oxidation cannot be negligible. However, the oxidation of MNZ was significantly decreased from approximately 85–55% by premixing 3 min and it was further decreased to 40% by premixing 6 min (Fig. 6a and b). This was due to the continuous consumption of radicals during the premixture of Mn-SAC and PMS. Such results further confirmed that MNZ oxidation was dominated by

radicals. In addition, leaching of Mn ions from the catalysts during the CP, CBZ, and MNZ oxidation was below  $5 \mu\text{g/L}$ , which showed negligible role to the homogeneous catalysis (Fig. S19). As a result, oxidation pathways for CP, CBZ, and MNZ in Mn-SAC/PMS system can be generally concluded as: (i) overwhelming electron-transfer oxidation of CP, (ii) electron-transfer-dominated oxidation of CBZ with the noticeable radical oxidation, and (iii) radicals-dominated oxidation of MNZ.

It was known that the open-circuit potentials of the catalysts might be changed after the addition of PMS and pollutants, which could intuitively reflect whether electron-transfer occurred in catalytic systems or participated in the oxidation of pollutants [55–57]. The initial oxidation potential ( $\sim 0.35 \text{ V}$ ) of Mn-SAC was significantly increased and kept stable at  $\sim 1.05 \text{ V}$  with the addition of 4 mM PMS (Fig. 6c), which was due to the formation of metastable intermediates (Mn-SAC/PMS\*) that elevated the potential of Mn-SAC [58]. This was also confirmed by the high PMS adsorption by the Mn-SAC with increasing PMS dosage (Fig. S20). The potential was then rapidly decreased to  $\sim 0.8 \text{ V}$  by adding the CP; this indicated that electron-transfer occurred between the Mn-SAC/PMS\* and CP. The addition of CBZ showed a weaker electron-transfer with the potential of Mn-SAC slightly decreasing from  $\sim 1.05 \text{ V}$  to  $\sim 0.95 \text{ V}$ , while no potential fluctuation was observed after the addition of MNZ (Fig. 6c). Such multiple electron-transfer results for different pollutants (e.g., CP, CBZ, and MNZ) were consistent with their versatile oxidation pathways. In addition, the open-circuit potentials of the Mn-SAC/PMS\* after the addition of different pollutants have been classified (Fig. 6c and d). As shown in Fig. 6d, the potentials before the addition of different pollutants were normalized according to the potential of MNZ to compare the reduced potentials after adding different pollutants, and three different descending trends can be observed. For example, the potentials of the Mn-SAC/PMS\* were significantly reduced by adding BPA and CP, which indicated that the oxidation of BPA and CP was dominated on the basis of a high electron-transfer process. An inferior descending trend was

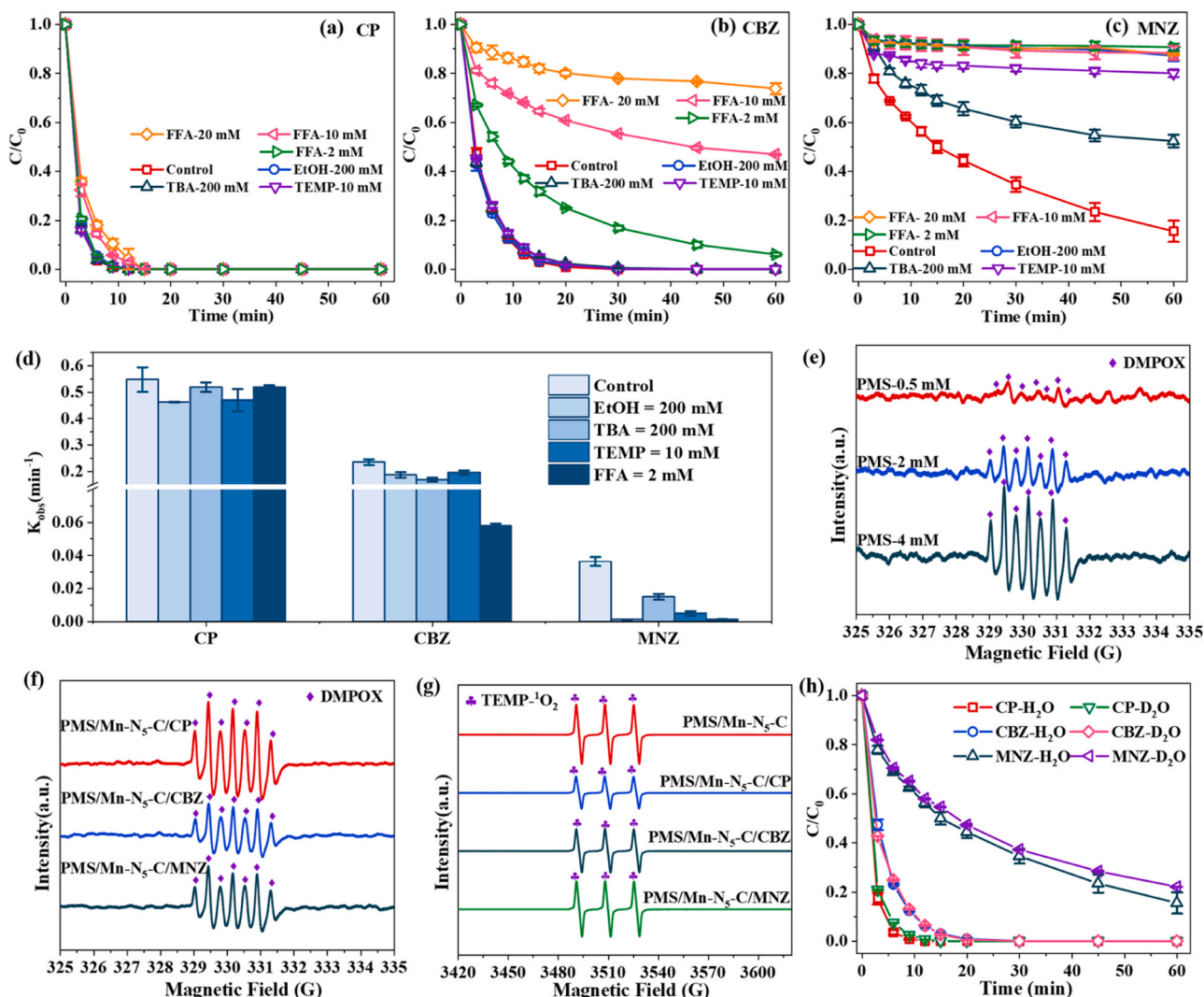


**Fig. 5.** (a) Quenching tests for typical pollutants (a) CP, (b) CBZ, (c) MNZ; (d)  $k_{obs}$  values for typical pollutants (CP, CBZ, and MNZ) under different quenching conditions; (e) DMPOX signals in Mn-SAC/PMS system at different PMS dosages; (f) DMPOX signals in Mn-SAC/PMS system with the addition of different pollutants; (g) TEMP-<sup>1</sup>O<sub>2</sub> signals in the Mn-SAC/PMS system with/without the addition of targeted pollutants; (h) CP, CBZ, and MNZ degradation in H<sub>2</sub>O and D<sub>2</sub>O solutions. (Catalyst dosage: 0.1 g/L; PMS dosage: 0.5–4.0 mM; pollutant concentrations: 10 mg/L).

then followed by adding SA, SMX, CBZ, and PNP, which showed a lower electron-transfer process. In contrast, no electron-transfer occurred by adding the CPL and MNZ. Intriguingly, the electron-transfer process in Mn-SAC/PMS system induced by different pollutants corresponded well to their  $\phi_{1/2}$  intervals (Fig. 6d). As a result, a good correlation between the redox potential characteristics of pollutants and their oxidation performances/pathways can be further confirmed.

Moreover, a galvanic oxidation system (GOS) was employed to further analyze the electron-transfer between targeted pollutants and Mn-SAC/PMS\* complex since the electrons can transfer from the pollutants to Mn-SAC/PMS\* complex along with electron channel if the dominated mechanism was based on electron shuttle [59]. PMS and pollutants were separated into two independent cells, which were connected by an agar salt bridge and an ampere meter, and Mn-SAC was coated on the graphite electrode (Fig. 6e). Significantly different current changes were detected when PMS and different pollutants were added into the PMS cell and pollutant cell. The addition of CP with low  $\phi_{1/2}$  could greatly stimulate the current to 225  $\mu$ A at 0.2 min and then gradually decreased to 60  $\mu$ A at 60 min (Fig. 6f). Similarly, CBZ with electron-rich group also promoted the current generation (Fig. 6f). In contrast, electron-deficient pollutants (like MNZ) with high  $\phi_{1/2}$  showed faint effect on the current formation due to their relatively inadequate

capacity in electron donation (Fig. 6f). These pollutants-related current formation results were consistent with the oxidation of pollutants in the GOS (Fig. S21), which further confirmed that the electron-transfer dominated Mn-SAC/PMS\* was less efficient in the oxidation of pollutants with high  $\phi_{1/2}$  values (e.g., MNZ).

### 3.5. DFT analysis

The molecular orbitals of different pollutants and Mn-SAC/PMS complexes were calculated via density functional theory (DFT) to determine electronic properties of targeted pollutants and catalysts [60]. Their molecular orbital (MO) energy diagrams were shown in Fig. 7a and 7b. The HOMO of pollutants (HOMO<sub>pollutants</sub>) were in the range of  $-5.908 \sim -7.295$  eV (Table S6), which were more negative than that ( $-3.263$  eV) of the LUMO of Mn-SAC/PMS complexes (LUMO<sub>Mn-SAC/PMS complexes</sub>); this was the premise of electron transfer from the HOMO of pollutants to LUMO of Mn-SAC/PMS complexes [61]. Results showed that a lower energy gap occurred between the LUMO of Mn-SAC/PMS complexes and HOMO of pollutants with lower  $\phi_{1/2}$  values (Fig. 7c and Table S6), which evidenced that electrons were easier to transfer from the lower  $\phi_{1/2}$  pollutants to Mn-SAC/PMS complexes, thus promoting the electron-transfer pathway for oxidizing the



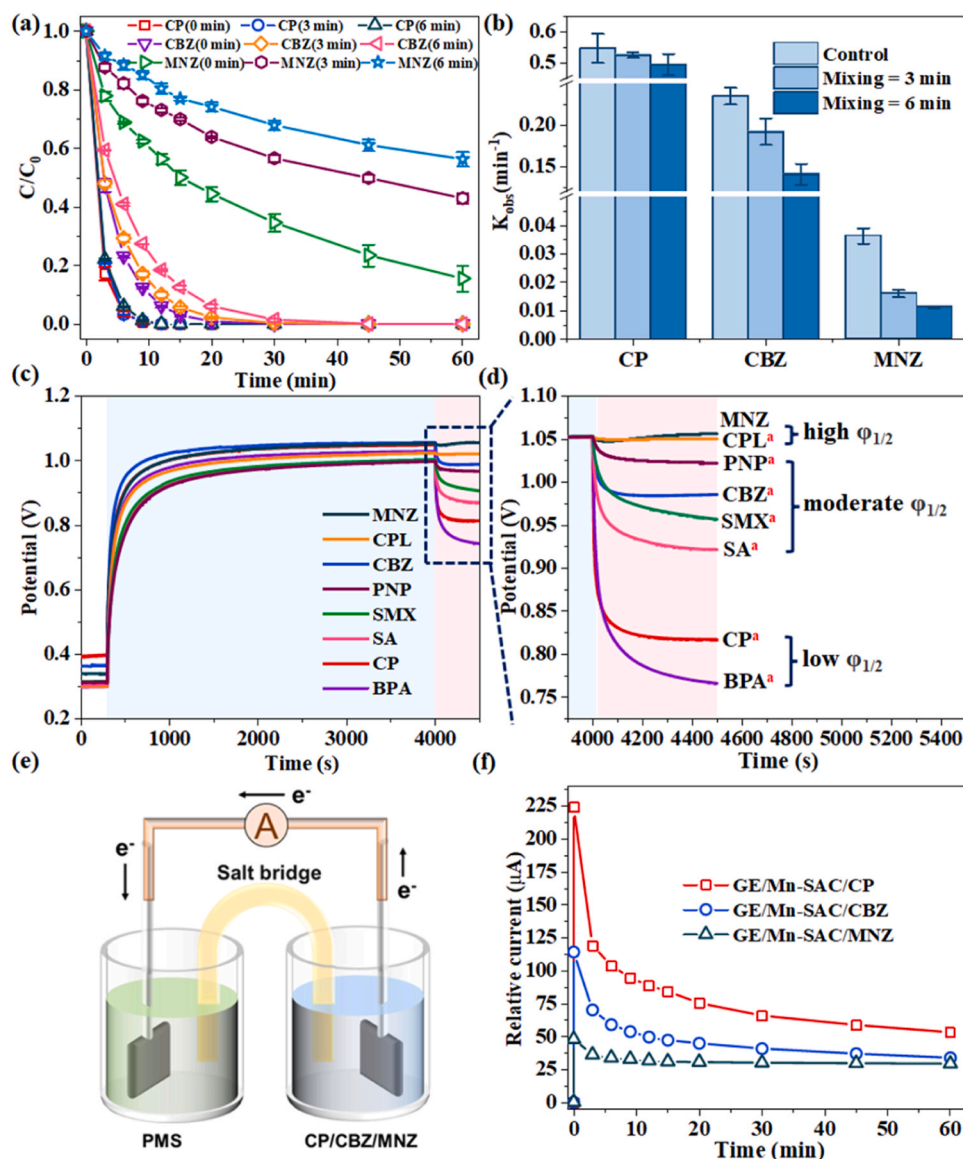


**Fig. 6.** (a) Oxidation of different pollutants in the Mn-SAC/PMS system via a premixing of Mn-SAC and PMS at designed time intervals; (b)  $k_{obs}$  values of different pollutants in the premixing tests (Catalyst dosage: 0.1 g/L; PMS dosage: 4.0 mM; pollutant concentrations: 10 mg/L); (c, and d) Open-circuit potential of Mn-SAC with the addition of different pollutants. (The superscripted a in d: the potentials before the addition of the above pollutants were normalized according to the potential of MNZ for comparing the reduced potentials after adding different pollutants); (e) GOS reaction device setup; and (f) current flowing from PMS cell to the pollutant cell in GOS.

targeted pollutants. As a result, a narrowed energy gap of  $LUMO_{(Mn-SAC/PMS \text{ complexes})}$  and  $HOMO_{pollutants}$  mean that the electron-transfer pathway was dominant in the Mn-SAC/PMS system, which could effectively oxidize the pollutants with lower  $\phi_{1/2}$ . In addition, there was a certain positive correlation between the energy gap and  $\ln k_{obs}$  of pollutants, and the correlation was better at higher PMS (Fig. 7d and Fig. S22). This phenomenon was also consistent with the fact that pollutants with lower  $\phi_{1/2}$  values always exhibited faster degradation rates via electron-transfer oxidation. Other electronic parameters (i.e., electrophilicity index, softness, hardness) of the pollutants were calculated (Table S5) [5,50], and correlated to the corresponding  $\phi_{1/2}$  values (Fig. 7e, and Fig. S23). The electrophilicity index reflecting the ability to accept electrons was also well correlated with the  $\phi_{1/2}$  values of pollutants and their  $\ln k_{obs}$  values (Fig. 7e, and Fig. S24). For example, CP with lower electrophilicity index exhibited lower capacity to accept electrons but stronger capacity to donate electrons, which showed a lower  $\phi_{1/2}$  value and higher  $\ln k_{obs}$  value; this confirmed that the CP was oxidized via electron transfer from CP molecule to the Mn-SAC/PMS\* complex [5,62]. Similarly, other organics (e.g. BPA, CBZ, SMX, SA) with electron-donating groups such as hydroxyl and amido groups exhibited lower redox potentials and were easily to be oxidized by the electron-transfer pathway. As a result, the

electron-transfer pathway was quite related to the redox potential of pollutants. In contrast, no correlations can be observed between the softness (or hardness) properties and  $\phi_{1/2}$  values of pollutants (Fig. S25). Overall, both the MO energy and electrophilicity index of pollutants reflected positive correlations with the  $\phi_{1/2}$  values of pollutants, which indicated the redox potential of pollutants was essential to the electron-transfer oxidation.

As for the radicals in Mn-SAC/PMS systems, the adsorption configuration of PMS onto the Mn-SAC was given in Fig. S26a. The length of peroxide O-O bond ( $L_{O-O}$ ) in the PMS was largely stretched to 1.449 Å after binding with Mn-SAC as compared with the free PMS of 1.434 Å (Fig. S26b). As a result, the Mn-SAC could promote the rupture of the peroxide O-O bond in the PMS to generate the radicals ( $SO_4^{\cdot-}$  or  $HO^{\cdot}$ ), which was not affected by the pollutants. In contrast, the electron-transfer oxidation was quite related to the redox potential ( $\phi_{1/2}$  values) of pollutants.

### 3.6. Degradation intermediates analysis

Degradation intermediates of CP, CBZ, and MNZ were detected and their oxidation pathways were diagrammed as shown in Fig. 8 and Fig. S27-29. Nonradical pathways (e.g.,  $^1O_2$ , high-valent metal-oxo,

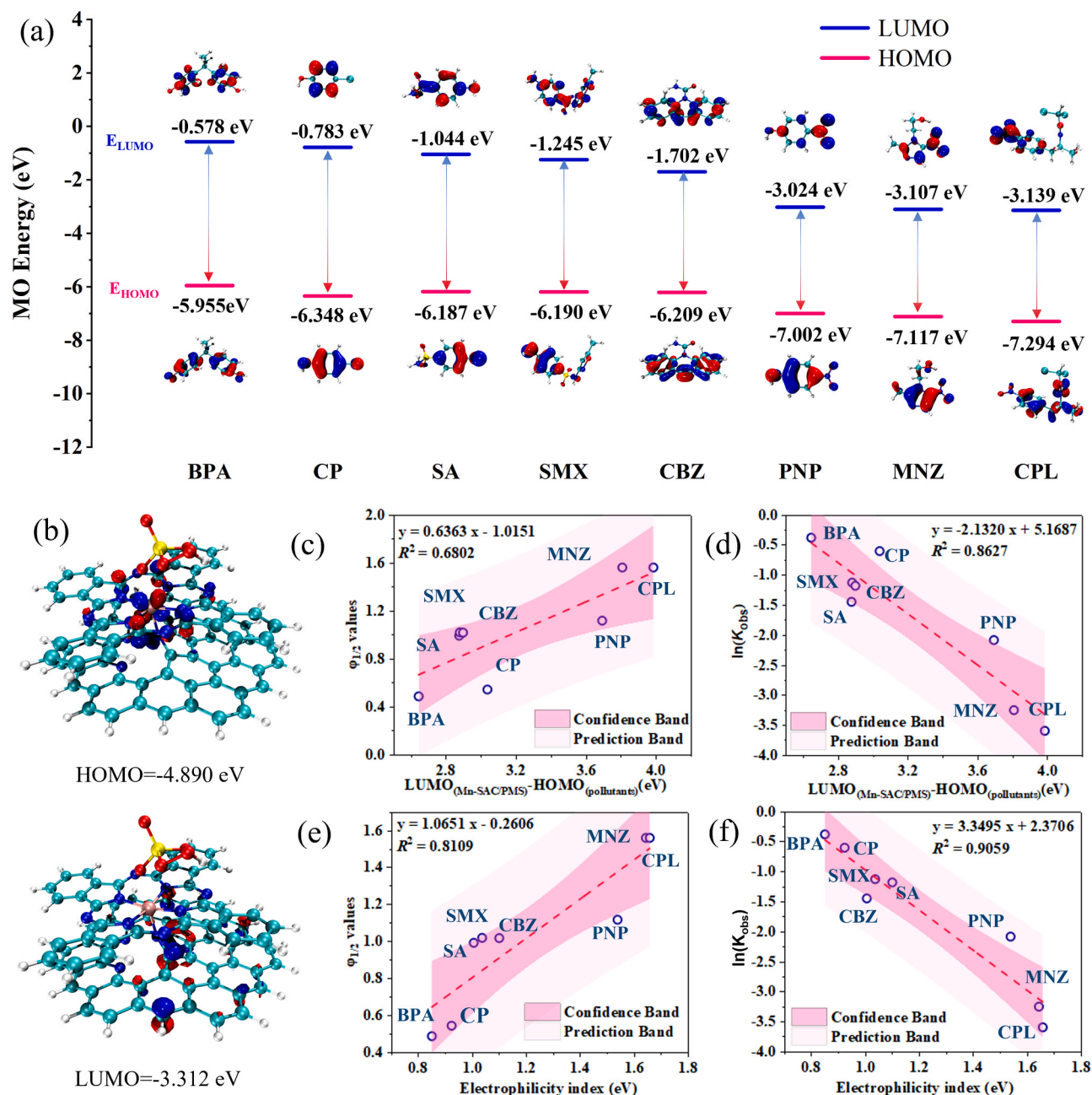


**Fig. 7.** (a) HOMO and LUMO of different pollutants; (b) HOMO and LUMO of Mn-SAC/PMS complexes; (c) Relationship between the energy gap of  $\text{LUMO}_{(\text{Mn-SAC/PMS complexes})}$  and  $\text{HOMO}_{\text{pollutants}}$  and  $\phi_{1/2}$  values of pollutants; (d) Relationship between the energy gap of  $\text{LUMO}_{(\text{Mn-SAC/PMS complexes})}$  and  $\text{HOMO}_{\text{pollutants}}$  and  $\ln K_{\text{obs}}$  values of pollutants obtained at PMS of 4.0 mM; (e) Relationship between the electrophilicity index and  $\phi_{1/2}$  values of pollutants; (f) Relationship between the electrophilicity index and  $\ln K_{\text{obs}}$  values of pollutants obtained at PMS of 4.0 mM.

electron-transfer oxidation) was prone to the oxidation of electron-donating groups [58]. As a result, the electron-donating hydroxyl groups and benzene ring in CP can be easily cleaved (Pa1-Pa3) by the electron-transfer oxidation (Fig. 8a). The electron-donating cyano groups and electron-withdrawing C=O groups both existed in the CBZ molecules. Electron-donating cyano groups in CBZ can be easily oxidized (Pb1, Pb3 and Pb6) by the dominated electron-transfer pathway in Mn-SAC/PMS/CBZ system (Fig. 8b). CBZ is prone to hydroxylation reactions due to the presence of  $\bullet\text{OH}$ , and  $-\text{NH}_2$  in CBZ readily oxidation reaction with  $\bullet\text{OH}$  or  $\text{SO}_4^{\cdot-}$  to form- $\text{NO}_2$ , the resulting product Pb5 is generated. Subsequently, Pb5 and other intermediates is continuously oxidized by  $\bullet\text{OH}$  or  $\text{SO}_4^{\cdot-}$  to products more C=O groups (Pb2, Pb4 and Pb7), followed by the electron-withdrawing C=O groups being decomposed (Pb8-Pb10). It was known that electron-transfer

pathway was inert to the electron-withdrawing groups [43,44], which indicated that the existed radicals in the Mn-SAC/PMS system participated to the oxidation of electron-withdrawing C=O groups. The electron-withdrawing nitro group in the MNZ was replaced (Pc1) by the radical-dominated pathway in Mn-SAC/PMS/MNZ system since nitro groups was reluctant to be oxidized by the electron-transfer pathway (Fig. 8c). Besides, The C=C unsaturated bonds in MNZ, in addition to being easily oxidized, was also attacked by  $\bullet\text{OH}$  or  $\text{SO}_4^{\cdot-}$  to opens the ring, resulting in the product Pc2 and Pc4-Pc5. Subsequently, Pc4-Pc5 is attacked by  $\bullet\text{OH}$  and undergo a carboxylation reaction (Pc6-Pc7). As a result, degradation intermediates of CP, CBZ, and MNZ further confirmed the versatile oxidation mechanisms for targeted pollutants.

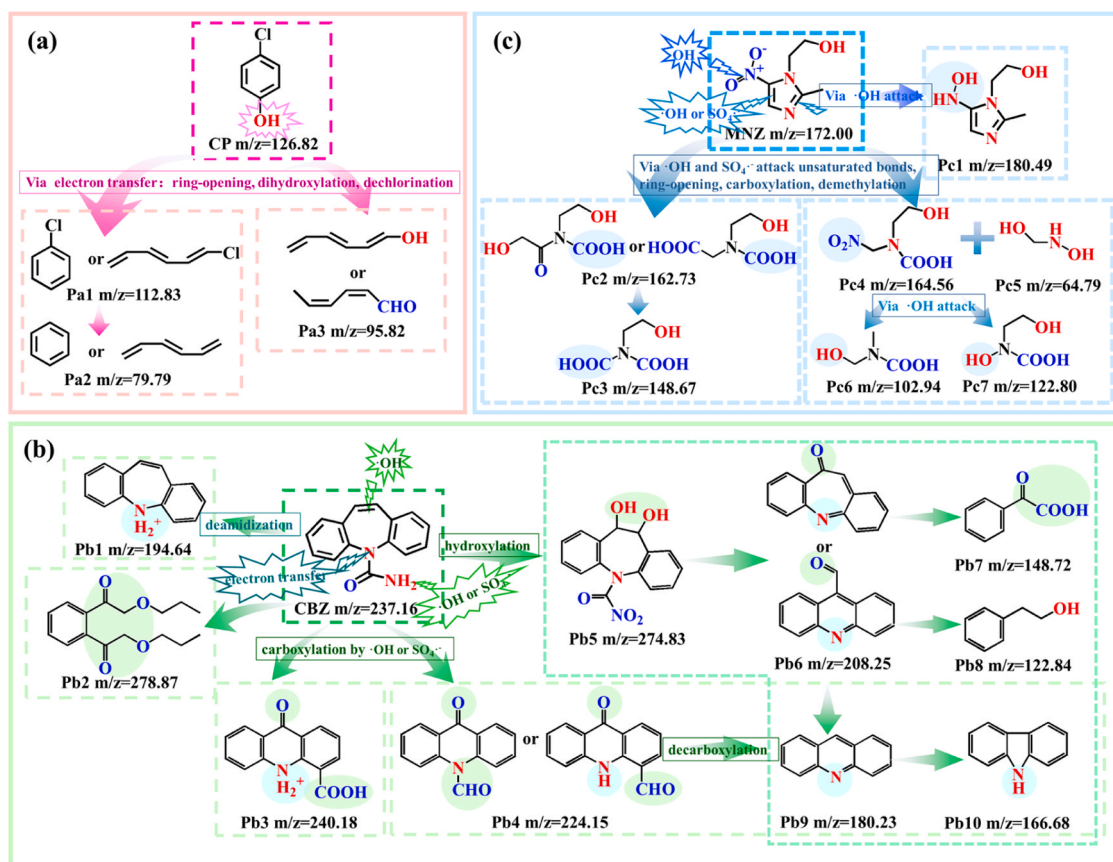


Fig. 8. Degradation intermediates and oxidation pathways of (a) CP, (b) CBZ, and (c) MNZ.

### 3.7. Degradation in catalytic filter systems

The degradation loss due to the coverage of intermediates on the surface of SACs is a common problem in the SACs/PMS systems which would greatly affect the cycle numbers. To solve this problem, a filter system via fixing the Mn-SAC on carbon felt was developed in this work to enhance the stability of Mn-SAC and overcome the reduced cycle numbers. The Mn-SAC was immobilized onto the carbon felt and packed in a column to prepare a catalytic filter system for the continuous oxidation of various pollutants (Fig. S30 and Fig. S31). The SEM of the Mn-SAC loaded filter showed dense fibrous structures with the fibrous diameter of 20–30  $\mu\text{m}$  (Fig. S32a and S32b), and its EDS mappings indicated that the Mn-SAC catalysts were well-dispersed on the surface of fibers (Fig. S32c). Degradation of different pollutants (e.g., CP and CBZ) with concentrations of 0.1–10 mg/L in the catalytic filter system was shown in Fig. S33a. Almost 100% of CP and CBZ oxidation could be constantly maintained for 210–240 min in the catalytic filter system. This result showed that Mn-SAC loaded catalytic filter system could make full use of the single atom Mn sites scattered on the carbon felt, and realized the continuous degradation of various pollutants. In addition, increasing the Mn-SAC loadings on the carbon felt could improve the continuous running of the catalytic filter, and complete oxidation of CBZ was elongated from 40 min to 210 min with the increase in the Mn-SAC loading from 5 mg to 15 mg (Fig. S33b). This was because with the increase of Mn-SAC loading, more single Mn sites could be formed in the catalytic filter to achieve efficient degradation of CBZ, and the Mn-SAC could rapidly intercept CBZ from flowing waters and bind PMS to excite both electron transfer and radical pathways for ultrafast CBZ degradation [63]. CBZ oxidation in Mn-SAC loaded catalytic filter system with the background of different anions were shown in Fig. S34. The results showed the complicated water matrixes only caused a very weak inhibition effect on the continuous degradation of CBZ, which indicated the

anti-interference of catalytic filter towards the external substances in water. In fact, phosphate surrounding condition could even promote the NPX degradation at pH 3.0–7.0 (Fig. S35), which was due to that phosphate could efficiently break the O=O bond of PMS to produce  $\text{SO}_4^{\bullet-}$  for degrading pollutants [64]. As a result, the Mn-SAC loaded catalytic filter system could exhibit a potential continuous operation in the Fenton-like catalytic systems.

## 4. Conclusions

The properties of pollutants in a complicated aquatic environment are always diverse. Therefore, understanding the origin of selective oxidation of versatile pollutants in ultrafast single-atom based Fenton-like system from the prospective of specific properties of pollutants will help to establish SACs/PMS systems with variable selectivity and tunable oxidation capacity for the organic decontamination. In this work, the selective degradation of eight pollutants via versatile pathways in single-atom based Fenton-like system was determined in a designed Mn-SAC/PMS system. Oxidation pathways for different pollutants in Mn-SAC/PMS system included: overwhelming electron-transfer oxidation for pollutants with low  $\phi_{1/2}$  values, electron-transfer-dominated oxidation with the noticeable radical oxidation for pollutants with moderate  $\phi_{1/2}$  values, and radicals-dominated oxidation for pollutants with high  $\phi_{1/2}$  values. This means that the ultrafast electron-transfer pathway was dominated for oxidizing targeted pollutants with a wide  $\phi_{1/2}$  interval in the Mn-SAC/PMS system. In addition, the positive correlation between the redox potential of pollutants and catalytic performances was strongly evidenced. Therefore, a thorough understanding on the selective oxidation law based on redox potential of pollutants was discerned in this work, which was of significance for popularizing the application of single atom catalysis for practical organic pollutant removal in water treatment systems. In



addition, the Mn-SAC based filter could rapidly intercept organics with different multiple concentrations from flowing waters and bind PMS to excite both electron transfer and radical pathways for ultrafast organics degradation, which exhibited a continuous operation of the Fenton-like systems for real application.

### CRediT authorship contribution statement

**Kexin Yin:** Methodology, Formal analysis, Investigation, Writing – original draft, Visualization. **Yanan Shang:** Visualization, Methodology. **DongDong Chen:** Formal analysis, Investigation. **Baoyu Gao:** Methodology. **Qinyan Yue:** Visualization.: XAS analysis, DFT calculation. **Xing Xu:** Resources, Writing – review & editing, Supervision.

### Declaration of Competing Interest

The authors declare that they have no known competing financial interests or personal relationships that could have appeared to influence the work reported in this paper.

### Data Availability

Data will be made available on request.

### Acknowledgments

The work was supported by National Natural Science Foundation of China (52170086) and Natural Science Foundation of Shandong Province (ZR2021ME013). The authors also want to thank Conghua Qi from Shiyanjia Lab (www.shiyanjia.com) for DFT calculations.

### Appendix A. Supporting information

Supplementary data associated with this article can be found in the online version at [doi:10.1016/j.apcatb.2023.123029](https://doi.org/10.1016/j.apcatb.2023.123029).

### References

- [1] K. Qian, H. Chen, W. Li, Z. Ao, Y.-n. Wu, X. Guan, Single-Atom Fe catalyst outperforms its homogeneous counterpart for activating peroxymonosulfate to achieve effective degradation of organic contaminants, *Environ. Sci. Technol.* 55 (2021) 7034–7043, <https://doi.org/10.1021/acs.est.0c08805>.
- [2] F. Chen, X.L. Wu, C.Y. Shi, H.J. Lin, J.R. Chen, Y.P. Shi, S.B. Wang, X.G. Duan, Molecular engineering toward pyrrolic N-Rich M-N<sub>4</sub> (M = Cr, Mn, Fe, Co, Cu) single-atom sites for enhanced heterogeneous fenton-like reaction, *Adv. Funct. Mater.* 31 (2021) 2007877, <https://doi.org/10.1002/adfm.202007877>.
- [3] L. Ge, Y. Yue, W. Wang, F. Tan, S. Zhang, X. Wang, X. Qiao, P.K. Wong, Efficient degradation of tetracycline in wide pH range using MgNCN/MgO nanocomposites as novel H<sub>2</sub>O<sub>2</sub> activator, *Water Res.* 198 (2021), 117149, <https://doi.org/10.1016/j.watres.2021.117149>.
- [4] R. Xiao, L. He, Z. Luo, R. Spinney, Z. Wei, D.D. Dionysiou, F. Zhao, An experimental and theoretical study on the degradation of clonidine by hydroxyl and sulfate radicals, *Sci. Total Environ.* 710 (2020), 136333, <https://doi.org/10.1016/j.scitotenv.2019.136333>.
- [5] R. Xiao, T. Ye, Z. Wei, S. Luo, Z. Yang, R. Spinney, Quantitative structure–activity relationship (QSAR) for the oxidation of trace organic contaminants by sulfate radical, *Environ. Sci. Technol.* 49 (2015) 13394–13402, <https://doi.org/10.1021/acs.est.5b03078>.
- [6] X. Li, X. Huang, S. Xi, S. Miao, J. Ding, W. Cai, S. Liu, X. Yang, H. Yang, J. Gao, J. Wang, Y. Huang, T. Zhang, B. Liu, Single cobalt atoms anchored on porous N-Doped graphene with dual reaction sites for efficient fenton-like catalysis, *J. Am. Chem. Soc.* 140 (2018) 12469–12475, <https://doi.org/10.1021/jacs.8b05992>.
- [7] Y. Shang, X. Xu, B. Gao, S. Wang, X. Duan, Single-atom catalysis in advanced oxidation processes for environmental remediation, *Chem. Soc. Rev.* 50 (2021) 5281–5322, <https://doi.org/10.1039/D0CS01032D>.
- [8] Y. Zong, X. Guan, J. Xu, Y. Feng, Y. Mao, L. Xu, H. Chu, D. Wu, Unraveling the overlooked involvement of high-valent cobalt-oxo species generated from the Cobalt(II)-Activated peroxymonosulfate process, *Environ. Sci. Technol.* 54 (2020) 16231–16239, <https://doi.org/10.1021/acs.est.0c06808>.
- [9] L. Peng, X.G. Duan, Y.N. Shang, B.Y. Gao, X. Xu, Engineered carbon supported single iron atom sites and iron clusters from Fe-rich Enteromorpha for Fenton-like reactions via nonradical pathways, *Appl. Catal. B Environ.* 287 (2021), 119963, <https://doi.org/10.1016/j.apcatb.2021.119963>.
- [10] M. Yang, Z. Hou, X. Zhang, B. Gao, Y. Li, Y. Shang, Q. Yue, X. Duan, X. Xu, Unveiling the origins of selective oxidation in single-atom catalysis via Co–N<sub>4</sub>-C intensified radical and nonradical pathways, *Environ. Sci. Technol.* 56 (2022) 11635–11645, <https://doi.org/10.1021/acs.est.2c01261>.
- [11] Y. Gou, P. Chen, L. Yang, S. Li, L. Peng, S. Song, Y. Xu, Degradation of fluoroquinolones in homogeneous and heterogeneous photo-Fenton processes: a review, *Chemosphere* 270 (2021), 129481, <https://doi.org/10.1016/j.chemosphere.2020.129481>.
- [12] J.P. Ribeiro, M.I. Nunes, Recent trends and developments in Fenton processes for industrial wastewater treatment – A critical review, *Environ. Res.* 197 (2021), 110957, <https://doi.org/10.1016/j.envres.2021.110957>.
- [13] C. Chu, J. Yang, X. Zhou, D. Huang, H. Qi, S. Weon, J. Li, M. Elimelech, A. Wang, J. H. Kim, Cobalt single atoms on tetrapyrrolic macrocyclic support for efficient peroxymonosulfate activation, *Environ. Sci. Technol.* 55 (2021) 1242–1250, <https://doi.org/10.1021/acs.est.0c06086>.
- [14] B. Liu, W. Guo, W. Jia, H. Wang, Q. Si, Q. Zhao, H. Luo, J. Jiang, N. Ren, Novel nonradical oxidation of sulfonamide antibiotics with Co(II)-Doped g-C<sub>3</sub>N<sub>4</sub>. Activated peracetic acid: role of high-valent cobalt-oxo species, *Environ. Sci. Technol.* 55 (2021) 12640–12651, <https://doi.org/10.1021/acs.est.1c04091>.
- [15] J. Pan, B. Gao, P. Duan, K. Guo, M. Akram, X. Xu, Q. Yue, Y. Gao, Improving peroxymonosulfate activation by copper ion-saturated adsorbent-based single atom catalysts for the degradation of organic contaminants: electron-transfer mechanism and the key role of Cu single atoms, *J. Hazard. Mater.* 9 (2021) 11604–11613, <https://doi.org/10.1039/D1TA02237G>.
- [16] P. Duan, X. Liu, B. Liu, M. Akram, Y. Li, J. Pan, Q. Yue, B. Gao, X. Xu, Effect of phosphate on peroxymonosulfate activation: accelerating generation of sulfate radical and underlying mechanism, *Appl. Catal. B Environ.* 298 (2021), 120532, <https://doi.org/10.1016/j.apcatb.2021.120532>.
- [17] J. Ma, N. Jia, C. Shen, W. Liu, Y. Wen, Stable cuprous active sites in Cu<sup>+</sup>-graphitic carbon nitride: structure analysis and performance in Fenton-like reactions, *J. Hazard. Mater.* 378 (2019), 120782, <https://doi.org/10.1016/j.jhazmat.2019.120782>.
- [18] J.-N. Zhu, X.-Q. Zhu, F.-F. Cheng, P. Li, F. Wang, Y.-W. Xiao, W.-W. Xiong, Preparing copper doped carbon nitride from melamine templated crystalline copper chloride for Fenton-like catalysis, *Appl. Catal. B Environ.* 256 (2019), 117830, <https://doi.org/10.1016/j.apcatb.2019.117830>.
- [19] Y. Mao, P. Wang, D. Zhang, Y. Xia, Y. Li, W. Zeng, S. Zhan, J.C. Crittenden, Accelerating Fe<sup>II</sup>-Aqua complex reduction in an efficient solid–liquid–interfacial fenton reaction over the Mn–CNH Co-catalyst at Near-Neutral pH, *Environ. Sci. Technol.* 55 (2021) 13326–13334, <https://doi.org/10.1021/acs.est.1c04534>.
- [20] J. Miao, Y. Zhu, J. Lang, J. Zhang, S. Cheng, B. Zhou, L. Zhang, P.J.J. Alvarez, M. Long, Spin-State-dependent peroxymonosulfate activation of single-atom M–N moieties via a radical-free pathway, *ACS Catal.* 11 (2021) 9569–9577, <https://doi.org/10.1021/acscatal.1c02031>.
- [21] X. Mi, P. Wang, S. Xu, L. Su, H. Zhong, H. Wang, Y. Li, S. Zhan, Almost 100% peroxymonosulfate conversion to singlet oxygen on single-atom CoN<sub>2+2</sub> sites, *Angew. Chem. Int. Ed.* 60 (2021) 4588–4593, <https://doi.org/10.1002/anie.202014472>.
- [22] Z. Yang, J. Qian, A. Yu, B. Pan, Singlet oxygen mediated iron-based Fenton-like catalysis under nanoconfinement, *Proc. Natl. Acad. Sci.* 116 (2019) 6659–6664, <https://doi.org/10.1073/pnas.1819382116>.
- [23] Y. Gao, Y. Zhu, Z. Chen, C. Hu, Nitrogen-coordinated cobalt embedded in a hollow carbon polyhedron for superior catalytic oxidation of organic contaminants with peroxymonosulfate, *ACS EST Engg.* 1 (2020) 76–85, <https://doi.org/10.1021/acsestengg.0c00039>.
- [24] J. Cai, B. Niu, H. Zhao, G. Zhao, Selective photoelectrocatalytic removal for group-targets of phthalic esters, *Environ. Sci. Technol.* 55 (2021) 2618–2627, <https://doi.org/10.1021/acs.est.0c07106>.
- [25] L.M. Wang, W.L. Chen, D.D. Zhang, Y.P. Du, R. Amal, S.Z. Qiao, J.W. Bf, Z.Y. Yin, Surface strategies for catalytic CO<sub>2</sub> reduction: from two-dimensional materials to nanoclusters to single atoms, *Chem. Soc. Rev.* 48 (2019) 5310–5349, <https://doi.org/10.1039/C9CS00163H>.
- [26] S. Wang, L. Xu, J. Wang, Iron-based dual active site-mediated peroxymonosulfate activation for the degradation of emerging organic pollutants, *Environ. Sci. Technol.* 55 (2021) 15412–15422, <https://doi.org/10.1021/acs.est.1c06205>.
- [27] Y. Li, T. Yang, S. Qiu, W. Lin, J. Yan, S. Fan, Q. Zhou, Uniform N-coordinated single-atomic iron sites dispersed in porous carbon framework to activate PMS for efficient BPA degradation via high-valent iron-oxo species, *Chem. Eng. J.* 389 (2020), 124382, <https://doi.org/10.1016/j.cej.2020.124382>.
- [28] Y. Yao, H. Yin, M. Gao, Y. Hu, H. Hu, M. Yu, S. Wang, Electronic structure modulation of covalent organic frameworks by single-atom Fe doping for enhanced oxidation of aqueous contaminants, *Chem. Eng. Sci.* 209 (2019), 115211, <https://doi.org/10.1016/j.ces.2019.115211>.
- [29] L. Yang, H. Yang, S. Yin, X. Wang, M. Xu, G. Lu, Z. Liu, H. Sun, Fe single-atom catalyst for efficient and rapid fenton-like degradation of organics and disinfection against bacteria, *Small* 18 (2022) 2104941, <https://doi.org/10.1002/sml.202104941>.
- [30] L.-S. Zhang, X.-H. Jiang, Z.-A. Zhong, L. Tian, Q. Sun, Y.-T. Cui, X. Lu, J.-P. Zou, S.-L. Luo, Carbon nitride supported high-loading Fe single-atom catalyst for activation of peroxymonosulfate to generate <sup>1</sup>O<sub>2</sub> with 100% selectivity, *Angew. Chem. Int. Ed.* 60 (2021) 21751–21755, <https://doi.org/10.1002/anie.202109488>.
- [31] M.X. Yang, R.X. Wu, S.S. Cao, Y.W. Li, S.S. Huo, W. Wang, Z. Hu, X. Xu, Versatile pathways for oxidating organics via peroxymonosulfate activation by different single atom catalysts confining with Fe–N<sub>4</sub> or Cu–N<sub>4</sub> sites, *Chem. Eng. J.* 451 (2023), 138606, <https://doi.org/10.1016/j.cej.2022.138606>.

- [32] J. Yang, D. Zeng, Q. Zhang, R. Cui, M. Hassan, L. Dong, J. Li, Y. He, Single Mn atom anchored on N-doped porous carbon as highly efficient Fenton-like catalyst for the degradation of organic contaminants, *Appl. Catal. B Environ.* 279 (2020), 119363, <https://doi.org/10.1016/j.apcatb.2020.119363>.
- [33] J. Chen, C. Fang, W. Xia, T. Huang, C.H. Huang, Selective transformation of beta-lactam antibiotics by peroxymonosulfate: reaction kinetics and nonradical mechanism, *Environ. Sci. Technol.* 52 (2018) 1461–1470, <https://doi.org/10.1021/acs.est.7b05543>.
- [34] T. Lu, Molclus program, Version 1.9.9.9, <http://www.keinsci.com/research/molclus.html>.
- [35] P.J. Stephens, F.J. Devlin, C.F. Chabalowski, M.J. Frisch, Ab initio calculation of vibrational absorption and circular dichroism spectra using density functional force fields, *J. Phys. Chem.* 98 (1994) 11623–11627, <https://doi.org/10.1021/j100096a001>.
- [36] M.J. Frisch, G.W. Trucks, H.B. Schlegel, G.E. Scuseria, M.A. Robb, J.R. Cheeseman, G. Scalmani, V. Barone, B. Mennucci, G.A. Petersson, 2009. Gaussian 09, Revision A.1, (2009).
- [37] T. Lu, F. Chen, Multiwfn: a multifunctional wavefunction analyzer, *J. Comput. Chem.* 33 (2012) 580–592, <https://doi.org/10.1002/jcc.22885>.
- [38] A.V. Marenich, C.J. Cramer, D.G. Truhlar, Universal solvation model based on solute electron density and on a continuum model of the solvent defined by the bulk dielectric constant and atomic surface tensions, *J. Phys. Chem. B* 113 (2009) 6378–6396, <https://doi.org/10.1021/jp810292n>.
- [39] X. Li, X. Yang, J. Zhang, Y. Huang, B. Liu, In Situ/Operando techniques for characterization of single-atom catalysts, *ACS Catal.* 9 (2019) 2521–2531, <https://doi.org/10.1021/acscatal.8b04937>.
- [40] D.H. Deng, X.Q. Chen, L. Yu, X. Wu, Q.F. Liu, Y. Liu, H.X. Yang, H.F. Tian, Y.F. Hu, P.P. Du, R. Si, J.H. Wang, X.J. Cui, H.B. Li, J.P. Xiao, T. Xu, J. Deng, F. Yang, P. N. Duchesne, P. Zhang, J.G. Zhou, L.T. Sun, J.Q. Li, X.L. Pan, X.H. Bao, A single iron site confined in a graphene matrix for the catalytic oxidation of benzene at room temperature, *Sci. Adv.* 1 (2015) 9, <https://doi.org/10.1126/sciadv.1500462>.
- [41] Y. Peng, B.Z. Lu, S.W. Chen, Carbon-supported single atom catalysts for electrochemical energy conversion and storage, *Adv. Mater.* 30 (2018) 25, <https://doi.org/10.1002/adma.201801995>.
- [42] C.Z. Wan, X.F. Duan, Y. Huang, Molecular design of single-atom catalysts for oxygen reduction reaction, *Adv. Energy Mater.* 10 (2020) 1903815, <https://doi.org/10.1002/aenm.201903815>.
- [43] W. Ren, L. Xiong, X. Yuan, Z. Yu, H. Zhang, X. Duan, S. Wang, Activation of peroxydisulfate on carbon nanotubes: electron-transfer mechanism, *Environ. Sci. Technol.* 53 (2019) 14595–14603, <https://doi.org/10.1021/acs.est.9b05475>.
- [44] W. Ren, C. Cheng, P. Shao, X. Luo, H. Zhang, S. Wang, X. Duan, Origins of electron-transfer regime in persulfate-based nonradical oxidation processes, *Environ. Sci. Technol.* 56 (2022) 78–97, <https://doi.org/10.1021/acs.est.1c05374>.
- [45] Y. Gao, Y. Zhou, S.-Y. Pang, J. Jiang, Y.-M. Shen, Y. Song, J.-B. Duan, Q. Guo, Enhanced peroxymonosulfate activation via complexed Mn(II): a novel non-radical oxidation mechanism involving manganese intermediates, *Water Res.* 193 (2021), 116856, <https://doi.org/10.1016/j.watres.2021.116856>.
- [46] H. Zhou, J. Peng, J. Li, J. You, L. Lai, R. Liu, Z. Ao, G. Yao, B. Lai, Metal-free black-red phosphorus as an efficient heterogeneous reductant to boost  $\text{Fe}^{3+}/\text{Fe}^{2+}$  cycle for peroxymonosulfate activation, *Water Res.* 188 (2021), 116529, <https://doi.org/10.1016/j.watres.2020.116529>.
- [47] B. Huang, Z. Xiong, P. Zhou, H. Zhang, Z. Pan, G. Yao, B. Lai, Ultrafast degradation of contaminants in a trace cobalt(II) activated peroxymonosulfate process triggered through borate: indispensable role of intermediate complex, *J. Hazard. Mater.* 424 (2022), 127641, <https://doi.org/10.1016/j.jhazmat.2021.127641>.
- [48] Y. Liu, Q. Lin, Y. Guo, J. Zhao, X. Luo, H. Zhang, G. Li, H. Liang, The nitrogen-doped multi-walled carbon nanotubes modified membrane activated peroxymonosulfate for enhanced degradation of organics and membrane fouling mitigation in natural waters treatment, *Water Res.* 209 (2022), 117960, <https://doi.org/10.1016/j.watres.2021.117960>.
- [49] Z. Wu, Y. Wang, Z. Xiong, Z. Ao, S. Pu, G. Yao, B. Lai, Core-shell magnetic  $\text{Fe}_3\text{O}_4@ \text{Zn}/\text{Co-ZIFs}$  to activate peroxymonosulfate for highly efficient degradation of carbamazepine, *Appl. Catal. B Environ.* 277 (2020), 119136, <https://doi.org/10.1016/j.apcatb.2020.119136>.
- [50] T. Ye, Z. Wei, R. Spinney, C.-J. Tang, S. Luo, R. Xiao, D.D. Dionysiou, Chemical structure-based predictive model for the oxidation of trace organic contaminants by sulfate radical, *Water Res.* 116 (2017) 106–115, <https://doi.org/10.1016/j.watres.2017.03.015>.
- [51] C. Chen, T. Ma, Y. Shang, B. Gao, B. Jin, H. Dan, Q. Li, Q. Yue, Y. Li, Y. Wang, X. Xu, In-situ pyrolysis of Enteromorpha as carbocatalyst for catalytic removal of organic contaminants: considering the intrinsic N/Fe in Enteromorpha and non-radical reaction, *Appl. Catal. B Environ.* 250 (2019) 382–395, <https://doi.org/10.1016/j.apcatb.2019.03.048>.
- [52] J. Miao, W. Geng, P.J.J. Alvarez, M.C. Long, 2D N-Doped porous carbon derived from polydopamine-coated graphitic carbon nitride for efficient nonradical activation of peroxymonosulfate, *Environ. Sci. Technol.* 54 (2020) 8473–8481, <https://doi.org/10.1021/acs.est.0c03207>.
- [53] R. Luo, M. Li, C. Wang, M. Zhang, M.A. Nasir Khan, X. Sun, J. Shen, W. Han, L. Wang, J. Li, Singlet oxygen-dominated non-radical oxidation process for efficient degradation of bisphenol A under high salinity condition, *Water Res.* 148 (2019) 416–424, <https://doi.org/10.1016/j.watres.2018.10.087>.
- [54] M. Zhang, R. Luo, C. Wang, W. Zhang, X. Yan, X. Sun, L. Wang, J. Li, Confined pyrolysis of metal-organic frameworks to N-doped hierarchical carbon for non-radical dominated advanced oxidation processes, *J. Mater. Chem. A* 7 (2019) 12547–12555, <https://doi.org/10.1039/C9TA02931A>.
- [55] W. Ren, L. Xiong, X. Yuan, Z. Yu, H. Zhang, X. Duan, S. Wang, Activation of peroxydisulfate on carbon nanotubes: electron-transfer mechanism, *Environ. Sci. Technol.* 53 (2019) 14595–14603, <https://doi.org/10.1021/acs.est.9b05475>.
- [56] X. Peng, J. Wu, Z. Zhao, X. Wang, H. Dai, Y. Wei, G. Xu, F. Hu, Activation of peroxymonosulfate by single atom Co-N-C catalysts for high-efficient removal of chloroquine phosphate via non-radical pathways: electron-transfer mechanism, *Chem. Eng. J.* 429 (2022), 132245, <https://doi.org/10.1016/j.cej.2021.132245>.
- [57] T. Ye, Z. Wei, R. Spinney, D.D. Dionysiou, S. Luo, L. Chai, Z. Yang, R. Xiao, Quantitative structure–activity relationship for the apparent rate constants of aromatic contaminants oxidized by ferrate (VI), *Chem. Eng. J.* 317 (2017) 258–266, <https://doi.org/10.1016/j.cej.2017.02.061>.
- [58] L. Peng, X. Duan, Y. Shang, B. Gao, X. Xu, Engineered carbon supported single iron atom sites and iron clusters from Fe-rich Enteromorpha for Fenton-like reactions via nonradical pathways, *Appl. Catal. B Environ.* 287 (2021), 119963, <https://doi.org/10.1016/j.apcatb.2021.119963>.
- [59] M. Luo, H. Zhang, P. Zhou, Z. Xiong, B. Huang, J. Peng, R. Liu, W. Liu, B. Lai, Efficient activation of ferrate(VI) by colloid manganese dioxide: comprehensive elucidation of the surface-promoted mechanism, *Water Res.* 215 (2022), 118243, <https://doi.org/10.1016/j.watres.2022.118243>.
- [60] Z. Wei, W. Li, D. Zhao, Y. Seo, R. Spinney, D.D. Dionysiou, Y. Wang, W. Zeng, R. Xiao, Electrophilicity index as a critical indicator for the biodegradation of the pharmaceuticals in aerobic activated sludge processes, *Water Res.* 160 (2019) 10–17, <https://doi.org/10.1016/j.watres.2019.05.057>.
- [61] P. Shao, S. Yu, X. Duan, L. Yang, H. Shi, L. Ding, J. Tian, L. Yang, X. Luo, S. Wang, Potential difference driving electron transfer via defective carbon nanotubes toward selective oxidation of organic micropollutants, *Environ. Sci. Technol.* 54 (2020) 8464–8472, <https://doi.org/10.1021/acs.est.0c02645>.
- [62] J. Lee, U. von Gunten, J.-H. Kim, Persulfate-based advanced oxidation: critical assessment of opportunities and roadblocks, *Environ. Sci. Technol.* 54 (2020) 3064–3081, <https://doi.org/10.1021/acs.est.9b07082>.
- [63] C. Zhu, Y. Nie, S. Zhao, Z. Fan, F. Liu, A. Li, Constructing surface micro-electric fields on hollow single-atom cobalt catalyst for ultrafast and anti-interference advanced oxidation, *Appl. Catal. B Environ.* 305 (2022), 121057, <https://doi.org/10.1016/j.apcatb.2021.121057>.
- [64] P. Duan, X. Liu, B. Liu, M. Akram, Y. Li, J. Pan, Q. Yue, B. Gao, X. Xu, Effect of phosphate on peroxymonosulfate activation: accelerating generation of sulfate radical and underlying mechanism, *Appl. Catal. B Environ.* 298 (2021), 120532, <https://doi.org/10.1016/j.apcatb.2021.120532>.